



# CHORUS

This is the accepted manuscript made available via CHORUS. The article has been published as:

## Mie scattering by soft core-shell particles and its applications to ellipsometric light scattering

Daniel J. Ross and Reinhard Sigel

Phys. Rev. E **85**, 056710 — Published 30 May 2012

DOI: [10.1103/PhysRevE.85.056710](https://doi.org/10.1103/PhysRevE.85.056710)

# Mie scattering by soft core-shell particles, and its applications to ellipsometric light scattering

Daniel J. Ross and Reinhard Sigel\*

*Adolph Merkle Institute, University of Fribourg, Fribourg, Switzerland*

(Dated: May 7, 2012)

Through the use of Mie theory generalized to multiple spheres, the derivatives of the scattering matrix elements and ellipsometric scattering variables are found as a function of shell thickness and nonconcentricity for core-shell particles. In particular, for the case of a core-shell sphere system where the centers are not concentric, the derivatives are taken with respect to the line segment describing the distance between spherical centers. The derivatives of the scattering matrix elements can be used to calculate the changes in ellipsometric light scattering, allowing for sensitivity and precision in quantitative models of fluctuations in core-shell systems. Computed results giving model contrast for a variety of sizes and fluctuation modes are used to design and guide novel light scattering experiments currently underway.

---

\* reinhard.sigel@guc.edu.eg, present address: German University in Cairo, Egypt

## I. INTRODUCTION

Developments in colloidal science have lead to greater control over different facets of interaction, such as stabilization [1, 2]. As these controls of stabilization often involve steric and electrosteric interactions through the addition of a polymeric interface, there is increased interest in studying the dynamics of this outer layer [3, 4].

As it is the softness of core-shell systems that makes them attractive for a number of applications, the ability of the mantle of such a composite particle to deform or fluctuate defines many of these useful properties [5–7]. It is desirable to be able to ascribe quantitative measures to the softness of the shell of a particle, as many of the interaction properties are related to the ability of the shell to deform [8]. For thin shells, usual spectroscopic methods should detect only the core of the particle and the equilibrium of the shell, which tends to produce a constant response to a probe, where the fluctuations of a configuration would often average out. If the derivatives of the observables in a characterization technique as a function of a fluctuating variable are known, however, it becomes possible to contrast small changes to the average or non-deformed case. The goal of this work, therefore, is to describe a theoretical method to model fluctuations of a shell in such a manner as to define possible contrast factor in the change of polarization, which can guide experimental measurement.

Thermal motion causes fluctuations of a shell, and there are additional possible situations that could cause deformation, or noncentricity, of a soft core-shell particle over a long time scale. For example, particles at an interface will deform if the coating material is energetically inclined towards one of the two materials [9]. Another possible configuration is through the formation of two or more particle clusters, where depending on the material and the interactions between the particles, the shell materials may deform away from, or toward other members of the cluster.

The issue of detecting and quantifying noncentricity in core-shell systems is difficult, as the changes in the scattering profile are almost negligible for measurements of scattering and absorption cross sections [10]. A candidate for detecting small changes in the relative positions of a core-shell system is ellipsometric light scattering (ELS), as it has been demonstrated to be very sensitive to changes in shell thickness and index of refraction [11–17].

The most simple model of a deformed core-shell particle is that of nonconcentric spheres, as seen in Fig. 1. A "hairy" colloidal particle, with hairs formed by polymer molecules is modeled as a spherical core-shell structure. Fluctuations and deformations in the soft shell leads to derivatives of scattering observables as a function of structural change. Although there is in practice a host of possible deformations, the most simple are those preserving the spherical nature of both the shell and core of the particle. Fluctuations or deformations of this type can be classed into two simple categories: symmetric, analogous to stretching or breathing type modes referred to as concentric fluctuations (CF), and asymmetric, which can be visualized by considering them as bending type vibrations, called nonconcentric fluctuations (NCF). For example, the well known volume phase transition of PNIPAM [11, 18] as a function of temperature can be considered a CF in this context. In contrast, the deformation due to an interaction force of a particle at an interface will cause the shell of a particle to distort more for regions closer to the interface, causing a NCF.

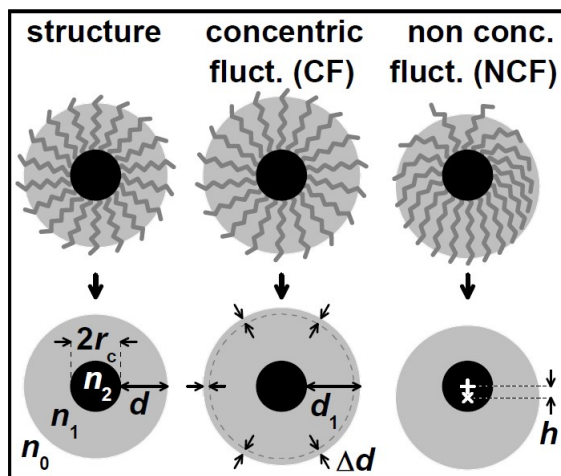


FIG. 1. Cartoon (upper) model of soft core-shell (lower) particle, where a hairy colloidal particle is represented by spheres. Refractive index changes from  $n_0$  in the external medium, to  $n_1$  in the shell of thickness  $d$ , to  $n_2$  in the core with a diameter of  $2r_c$ . In concentric fluctuations (middle) the shell thickness changes by  $\Delta d$ , while nonconcentric fluctuations (right) are characterized by the offset  $h$  between the centres of the core  $+$  and the shell  $\times$ .

In either case fluctuation or deformation, as long as the products can be considered relatively spherical, the scattering can be modeled analytically. In the case of CF, the usual descriptions of concentric spheres can be used [19]. For NCF, two spheres with centers located at different origins are required, a case not covered by the standard derivations of Mie's solution to scattering by spheres.

The theory of scattering by a spherical object has an ambiguous history, in terms of who developed the first full solution, as detailed by Kerker [20] and more recently by Bohren and Huffman [19]. While the contributions of Lorenz and Debye are not neglected, here it will be referred to as the solution by Mie [21], for brevity. The basic Mie solution to the problem has been extended in a number of different ways, including that of concentrically layered spheres, which has been thoroughly described in excellent detail [19, 20]. A generalization of this approach, the problem of nonconcentricity has been described theoretically by a number of authors [22–26], through the use of scattering by multiple spheres, although to our knowledge this is the first work examining the derivatives of scattering parameters as a function of nonconcentricity. Recently, analytic differentiation of scattering observables for nonspherical particles has been done. [27, 28]. The problem of nonconcentric spheres has also been examined recently [29, 30] for large spheres and inclusions, with examination of both resonance dependence on size and shape as well as spatial distribution of fields.

Scattering by nonconcentric spheres is related to the formalism of scattering by multiple spheres. The mathematical development of the translation coefficients for the vector spherical harmonics [31–33] allowed for the exact calculation by multiple spheres. This critical advance made possible a tractable methodology for comparison of experiment and theory for important cases such as bispheres and higher order clusters. Aggregated and similar multibodied cases could be modeled exactly, allowing better prediction for systems in which interaction can be a strong contributor, or even the driving factor, such as in surface enhanced phenomena [34]. The early work in the field of scattering by multiple objects considered only external aggregation [35], a trend that is continued today, although extended to allow for arbitrary configurations, optical properties, and beamshape [36, 37], closing the gap between experimental measurement and idealized simulation. The bulk of the use of these theories is directed towards cluster characterization, but only fairly small changes are required to allow the theory of multiple scattering to be utilized in the case of internal aggregation, or nonconcentric core-shell particles [38].

The purpose of this paper is to describe the fluctuations of the scattering of a soft core-shell system considering either the expansion of the shell, or the relative motion of the inclusion to the host, through computation of the derivatives of the scattering coefficients with respect to displacement or shell thickness. With known derivatives of scattering coefficients, it is then possible to compute the derivatives of almost any scattering phenomena, such as cross sections, scattered fields, or angular intensities. In the case of NCF, the principle idea is to first assume that the system is at the concentric point, and use the scattering coefficients at this trivial point to bootstrap upwards to the first derivative. Repeated bootstrapping allows for calculation of higher order derivatives and scattering coefficients at any displacement through the use of a Taylor expansion.

Section II. describes the model for the computation of analytic derivatives for fluctuating spheres. Section II. A. discusses, in particular, differentiation of the ELS observables written generally to allow for use with any variable, and holds for both CF and NCF. Section II. B. highlights the use of a dynamic contrast change in the case of the CF. Section II. C contains the model used for scattering by nonconcentric spheres. The model is based on a reference frame fixed to the laboratory frame, and the full solution for scattering and the derivatives of scattering observables can be compared immediately to experimental results, without further rotation. The novel bootstrap method allows the calculation of all orders of differentiation of scattering observables during fluctuations about equilibrium, without matrix inversions or any other further computational costs beyond that of the nonconcentric model.

Section III discusses computed ellipsometric scattering results for the model of fluctuating spheres. Optical properties are used for the model system of polystyrene spheres in water, surrounded by a swollen polymer shell. The ELS in the equilibrium case is seen in Section III. A. The behavior of the scattering is discussed in detail to provide an understanding of the rich structure appearing in the derivatives. Concentric fluctuations are described in Section III. B, and nonconcentric follows in III. C, for the same sizes and optical properties used for the equilibrium case.

## II. METHODOLOGY

The optical parameters used throughout are illustrated in Fig. 1. The index of refraction of the medium surrounding the scattering system is labeled  $n_0$ , and the indices of refraction of the shell and core of the scatterer are labeled  $n_1$  and  $n_2$  respectively. The radius of the core is given by  $r_c$ , and the equilibrium thickness of the shell as  $d$ . In the case of NCF, the distance between the centers, or the magnitude of the nonconcentricity, is labeled  $h$ . For CF, the thickness changes to  $d_1 = d + \Delta d$ , and  $n_1$  is adapted in a way to keep the total amount of swollen polymer in the shell constant.

The mechanics of finding the derivatives of ellipsometric light scattering parameters is divided into three sections.

In the first, the derivatives of the Jones matrix elements and ellipsometric variables themselves are discussed. These results can be applied to both CF and NCF. The second part briefly discusses concentric fluctuations, in particular the change in optical contrast due to expansion of the shell. In this case, derivatives of the Mie coefficients of a core-shell system [19] are taken with respect to shell thickness. The third section deals with finding the derivatives of the scattering coefficients as a function of nonconcentricity.

### A. Derivatives of Jones Matrix Elements and Ellipsometric Variables

The Jones matrix elements  $S_n$  express the relationship between the incident  $E^{\text{inc}}$  and scattered  $E^{\text{sca}}$  fields. Within the Jones formalism, the polarization dependent scattering is given by [14]:

$$\begin{pmatrix} \mathbf{E}_H^{\text{sca}} \\ \mathbf{E}_V^{\text{sca}} \end{pmatrix} = \frac{e^{ikr_1}}{-ikr_1} \begin{pmatrix} S_2 & S_4 \\ S_3 & S_1 \end{pmatrix} \begin{pmatrix} \mathbf{E}_H^{\text{inc}} \\ \mathbf{E}_V^{\text{inc}} \end{pmatrix}, \quad (1)$$

where  $r_1$  is the distance to the detector, and  $k = n_0 k_0$  where  $k_0 = 2\pi/\lambda$  is the wavenumber in vacuum, and the subscripts  $H$  and  $V$  refer to the field components in and perpendicular to the scattering plane, respectively.

In eq. (1),  $S_3$  and  $S_4$  represent depolarized contributions. In the case of spherical particles, these terms are zero. For NCFs that are either in the scattering plane, or perpendicular to it, there is no depolarization as well, so the first order terms in a Taylor expansion of  $S_3$  and  $S_4$  vanish. Depolarization is thus a second order effect and is not considered here.

For simplicity, the exit of the scattered light from the scattering medium is not discussed here. In experiments with a cylindrically symmetric scattering geometry, there is a transmission correction only, which cancels in a calibration step, as it affects all  $S_n$  equally.

In analogy to classical ellipsometry, ellipsometric light scattering (ELS) measures the quotient of the scattering amplitudes parallel and perpendicular to the scattering plane,  $S_2$  and  $S_1$ . The complex ellipsometric quotient is defined as:

$$\rho = \frac{S_2}{S_1} = \tan \Psi e^{i\Delta}. \quad (2)$$

As the Jones matrix elements are complex,  $\rho$  is also a complex number with phase  $\Delta$  and the amplitude ratio  $\tan \Psi$  [14].

In order to obtain the fluctuation contrast factors which are the derivatives of these ellipsometric scattering parameters, the formal derivative of the complex ellipsometric quotient is taken.  $\rho'$  here can refer to derivatives with respect to shell thickness  $d$  or the nonconcentricity  $h$ , and applies to both CF and NCF.

$$\rho' = \frac{S_1 S_2' - S_2 S_1'}{S_1^2} \quad (3)$$

The logarithmic derivative of the complex ellipsometric ratio is:

$$(\ln \rho)' = \frac{\rho'}{\rho} = \frac{(\tan \Psi)'}{\tan \Psi} + i\Delta'. \quad (4)$$

The derivative of the phase can therefore be computed by:

$$\Delta' = \text{Im}\left(\frac{\rho'}{\rho}\right) \quad (5)$$

With the derivative of the phase calculation, the derivative of the amplitude is found by:

$$(\tan \Psi)' = \rho' e^{-i\Delta} - i\Delta' \tan \Psi \quad (6)$$

The values of the imaginary part of the complex ellipsometric ratio are generally very small, and therefore the branch cuts of the phase are not a concern. When the real part of  $\rho$  approaches zero, causing a minimum in  $\tan \Psi$  [15],  $\Delta$  will pass through  $\pm 90^\circ$ , while  $\Delta'$  will go to large values.

### B. Derivatives with Respect to Shell thickness

The CF, or symmetric fluctuation is modeled as an expansion or contraction of the shell thickness. The fluctuation of the shell can be thought of as an expansion or contraction of the polymeric hairs surrounding the particle. As the shell fluctuates, there is a change in the index of refraction as the same amount of material occupies a different amount of space, causing a change in contrast as the size changes.

The derivative of the ellipsometric ratio can be expressed as:

$$\frac{d}{dd_1}\rho(d, n_1(d_1)) = \frac{\partial\rho}{\partial d_1} + \frac{\partial\rho}{\partial n_1} \frac{dn_1}{dd_1} \quad (7)$$

Expressing the shell thickness at equilibrium as  $d$ , and the thickness during some fluctuation as  $d_1$ , the index of refraction can be expressed as:

$$n_1(d_1) = n_0 + (n_1 - n_0) \frac{V(d)}{V(d_1)} \quad (8)$$

$$= n_0 + (n_1 - n_0) \frac{(r_c + d)^3 - r_c^3}{(r_c + d_1)^3 - r_c^3} \quad (9)$$

Taking the derivative with respect to the fluctuating shell thickness  $d_1$  and evaluating at the equilibrium thickness  $d$  gives:

$$\left. \frac{dn_1(d)}{dd_1} \right|_{d_1=d} = -(n_1 - n_0) \frac{3(r_c + d)^2}{(r_c + d)^3 - r_c^3} \quad (10)$$

Although taking the derivative adds complication to the equations, the mathematics are essentially the same as in the description of the core-shell geometry without fluctuations, excepting that second derivatives of the Riccati-Bessel functions must also be calculated.

### C. Nonconcentric Scattering

As this case deals with embedded particles, multiple spherical coordinate systems are required, relating the incident light to the particle's orientation, the geometrical relationship between the scattering particles, and lastly, the position of the detector in the frame of the incident light and the particle system. For the purposes of this work, a scattering plane is defined as the plane containing the incident light and the detector, and the positions of the scatters can then be discussed in a Cartesian system. The scattering plane is defined to contain the  $xz$  axes, as shown in Fig. 2.

To make the relationship between the scattering and laboratory frames as simple as possible, the incident light,  $I_0$  is considered to be directed in the  $+z$  direction, and the scattered light to be outgoing from an angle  $\Theta$  in the scattering plane, such that  $\Theta$  represents the azimuthal angle in the usual definition of spherical coordinates. The horizontal component of the incident electric field  $E_H^{\text{inc}}$  is pointed in the  $\hat{\Theta}$  direction, in the scattering plane, and lies in the  $xz$  plane. The vertical components of incident  $E_V^{\text{inc}}$  and scattered fields  $E_V^{\text{sca}}$  is in the  $\hat{\Phi}$  direction. The choice of fixing the coordinate system to the incident light, and allowing arbitrary sphere positions allows for a clear correlation between the laboratory and model systems.

The method here follows the formalism proposed by Fuller [24, 38], as the Order of Scattering (OS) methodology is highly convenient for examination of derivatives. The theory is briefly reproduced here to note the changes involved due to differentiation and as well for consistency regarding ellipsometric scattering. The OS method describes the scattering by multiple spheres through following scattering events systematically, and finding the scattering by the whole system through an iterative approach.

Within the reference frame defined by the scattering plane, the core of the particle is shifted relative to the shell in the cardinal directions. Shifting of the core rather than the shell is a slight computational aid, in that the coefficients of expansion of the plane wave do not need to be adjusted for the relative phase change, and as well, as the radiating particle is the shell, the outgoing waves are also centered at the origin. First, the incident field can be described through the product of the spherical expansion coefficients of the plane wave, given by  $p_{mnp}(\gamma)$ . A time dependence of  $\exp(-i\omega t)$  is implicit throughout. Here,  $\gamma$  is the angle between the scattering plane and the incident electric field.

$$E^{\text{inc}} = \sum_{n=1}^{\infty} \sum_{m=-n}^n \sum_{p=1}^2 p_{mnp}(\gamma) N_{mnp}^{(1)}, \quad (11)$$

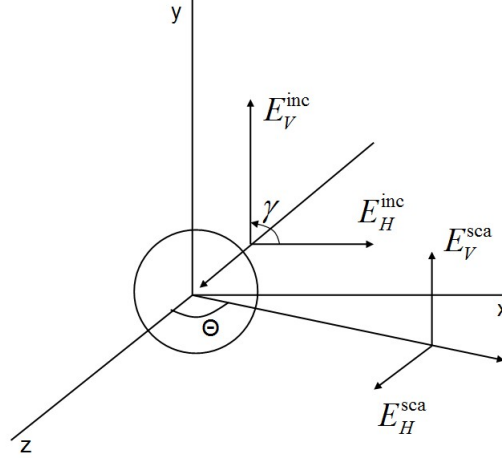


FIG. 2. Scattering geometry. Relationship between the incident light, and light scattered at angle  $\Theta$ , and the Cartesian coordinates describing nonconcentricity

where  $N_{mnp}^{(1)}$  are the vector spherical harmonics (VSH), and the superscript of (1) for the VSH refers to the use of spherical Bessel functions of the first kind,  $j_n(kR)$  [39], which remain finite at the origin. The indices  $m$  and  $n$  are the separation constants. The index  $p$  refers to the two different solutions of the vector wave equation, often expressed as  $\mathbf{N}$ , or transverse electric (TE), and  $\mathbf{M}$ , or transverse magnetic (TM) for  $p = 1$  and  $p = 2$  respectively. In spherical coordinates, the electric field in the TE mode points in the  $\hat{\Phi}$  direction, and in the  $\hat{\Theta}$  direction in the TM case. The expansion coefficients and VSH are detailed in the appendix. Similarly, the scattered field can be expressed as:

$$E^{sca} = \sum_{m,n,p} a_{mnp}(\gamma) N_{mnp}^{(3)}. \quad (12)$$

In the case of the scattered field, the superscript (3) indicates the use of the spherical Bessel functions of the third kind,  $h_n(kR)$ , which give the correct decay as  $kR \rightarrow \infty$  [20]. The  $a_{mnp}$  are scattering coefficients of the shell, where the scattering contribution from the core has been accounted for. They differ from the usual Mie coefficients [19, 20] in that the nonconcentricity introduces a break from spherical symmetry. This demands that the separation constant  $m$  is no longer trivial, and as well, the scattering coefficients are a function of incident polarization  $\gamma$ .

The order of scattering method is represented in Fig. 3. The electric field of the incident light is found through the spherical expansion  $p_{mnp}$ . The 0<sup>th</sup> order of scattering is identical to that of a simple sphere. The scattered and internal field coefficients are given by  ${}^0a_{mnp}^1 = \bar{a}_{np}^1 p_{mnp}$  and  ${}^0c_{mnp}^1 = \bar{c}_{np}^1 p_{mnp}$ , respectively, where  $\bar{a}_{np}^1$  and  $\bar{c}_{np}^1$  are the Mie coefficients for the shell in the external medium, reproduced in the appendix.

The superscript  $j = 0..∞$  preceding the scattering coefficients  ${}^j a_{mnp}^l$  indicates the order of scattering, and the superscript following  $l = 1, 2$  denotes the sphere from which the last scattering event occurred. As before, the subscripts index the separation variables involved.

The internal field then scatters from the core resulting in  ${}^1 a_{mnp}^2$ , which may further scatter externally,  ${}^1 a_{mnp}^1$ , or internally,  ${}^1 c_{mnp}^1$ . In general, the set of equations for the scattering coefficients is done through recursion through the order of scattering, denoted by index  $j$ :

$${}^j a_{mnp}^2 = \bar{a}_{np}^2 \sum_{\mu\nu q} {}^{j-1} c_{\mu\nu q}^1 \tilde{A}_{mnp\mu\nu q}^{21} \quad (13)$$

$${}^j a_{mnp}^1 = \hat{c}_{np}^1 \sum_{\mu\nu q} {}^j a_{\mu\nu q}^2 \tilde{A}_{mnp\mu\nu q}^{12} \quad (14)$$

$${}^j c_{mnp}^1 = \hat{a}_{np}^1 \sum_{\mu\nu q} {}^j a_{\mu\nu q}^2 \tilde{A}_{mnp\mu\nu q}^{12} \quad (15)$$

where the Mie coefficients marked with the caret ( $\hat{a}_{np}^1$  and  $\hat{c}_{np}^1$ ), detailed in the appendix, represent the reflection and refraction through the concave spherical boundary of the shell particle [38]. The terms  $\tilde{A}_{mnp\mu\nu q}^{\ell\ell'}$  are the translation

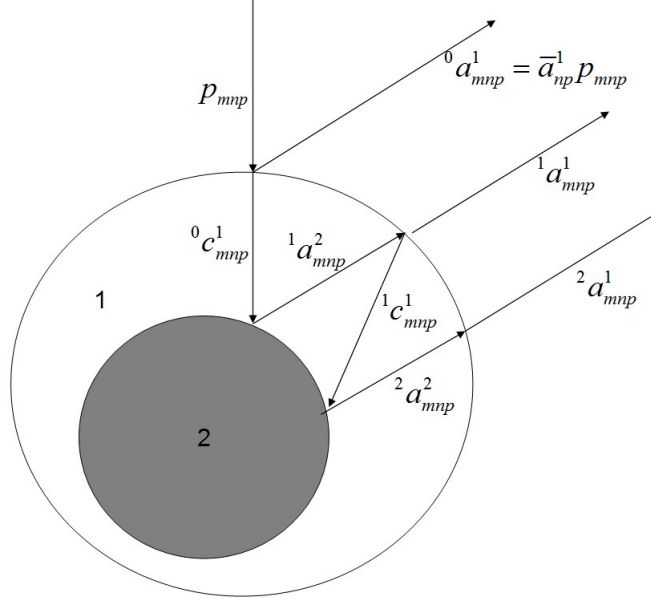


FIG. 3. Visualization of order of scattering for nonconcentric spheres, described in text.

terms of the vector spherical harmonics, which, when scaled by the appropriate Mie coefficient, moves the waves scattered off of sphere  $\ell'$  into the frame of reference frame of sphere  $\ell$ . These translation coefficients are also discussed in the appendix. It is worthwhile stressing that rather than the usual definition of the Mie coefficients, the scattering coefficients  $a_{mnp}$  include the vector nature, as they are proportional to the incident field expansion coefficients. Finally, the total scattering coefficient is found through the sum of the order of scattering terms,

$$a_{mnp}(\gamma) = \sum_{j=0}^{\infty} j a_{mnp}^j(\gamma) \quad (16)$$

where  $\gamma$  is the polarization of the incident field relative to the scattering plane.

The method to find the derivatives  $\frac{d}{dh}$  of the nonconcentric scattering coefficients becomes simplified when the concentric scattering coefficients are calculated first. As the usual Mie coefficients and, for the case of the shell located at the origin, the plane wave expansion coefficients, do not depend on  $h$  the first derivatives of the 0'th OS terms are zero,  ${}^0 a_{mnp}^1 = 0$  and  ${}^0 c_{mnp}^1 = 0$ . The translation coefficients of the vector spherical harmonics, however, depend on  $h$ , and the derivatives are nonzero, implying that scattering coefficients higher than the 0'th order also depend on the nonconcentricity.

As the computation of the translation coefficients of the vector spherical harmonics is the most intensive, approximating the full translation function through a Taylor expansion about zero makes the problem tractable.

A general form of the  $\nu$ 'th derivative of the scattering coefficients for arbitrary order of scattering  $j$  can be written through the use of the binomial expansion of the derivative of products:

$$({}^j a_{mnp}^2)^\nu = \bar{a}_{np}^2 \sum_{\mu\nu q} \sum_{\kappa=0}^{\nu} \binom{\nu}{\kappa} ({}^{j-1} c_{\mu\nu q}^1)^{\nu-\kappa} (\tilde{A}_{mnp\mu\nu q}^{21})^\kappa \quad (17)$$

$$({}^j a_{mnp}^1)^\nu = \hat{c}_{np}^1 \sum_{\mu\nu q} \sum_{\kappa=0}^{\nu} \binom{\nu}{\kappa} ({}^j a_{\mu\nu q}^2)^{\nu-\kappa} (\tilde{A}_{mnp\mu\nu q}^{12})^\kappa \quad (18)$$

$$({}^j c_{mnp}^1)^\nu = \hat{a}_{np}^1 \sum_{\mu\nu q} \sum_{\kappa=0}^{\nu} \binom{\nu}{\kappa} ({}^j a_{\mu\nu q}^2)^{\nu-\kappa} (\tilde{A}_{mnp\mu\nu q}^{12})^\kappa \quad (19)$$

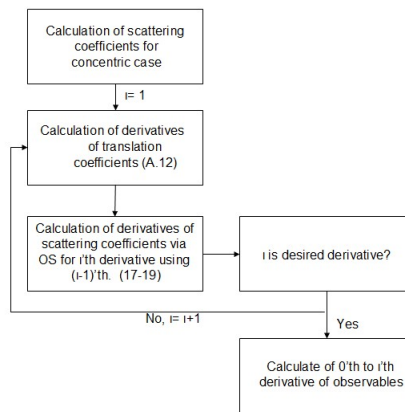


FIG. 4. Schematic of bootstrap method of calculation.

To calculate up to arbitrary order of derivatives, the Mie coefficients for the concentric case are first calculated, using either a standard method for core-shell particles [19], or the formalism described here. The first derivative can then be computed using these concentric results with the additional terms required due to interaction coefficients that are a function of  $h$ , proceeding using the OS method to obtain all necessary derivatives of scattering coefficients. The second derivative will involve both the equilibrium results and first derivatives, and similarly for higher orders, as displayed in Fig. 4

Through the order of scattering method, the scattering by the shell implicitly includes the contributions from the core. Calculation of the two required polarizations is done separately, with  $\gamma = 0^\circ$  and  $\gamma = 90^\circ$ , corresponding to horizontal and vertical polarization, respectively. The Jones matrix elements are then:

$$S_1 = \frac{i}{k} \sum_{n,m} (-i)^n [\pi_{mn}(\theta) a_{mn1}(90^\circ) + \tau_{mn}(\theta) a_{mn2}(90^\circ)], \quad (20)$$

$$S_2 = \frac{i}{k} \sum_{n,m} (-i)^{n+1} [\tau_{mn}(\theta) a_{mn1}(0^\circ) + \pi_{mn}(\theta) a_{mn2}(0^\circ)], \quad (21)$$

where  $a_{mnp}(0^\circ)$  and  $a_{mnp}(90^\circ)$  are the scattering coefficients calculated with incident polarization  $\gamma = 0^\circ$  and  $\gamma = 90^\circ$  respectively.

Mie terms are calculated to the order  $x + 4x^{1/3} + 4$ , with the size parameter  $x = k(r_c + d)$  [19]. In the order of scattering method, the number of OS terms is set equal to the number of Mie terms, which gives good convergence for the optical parameters used. Programs to calculate the scattering by nonconcentric spheres are verified by comparison to previous work [23] and available discrete dipole approximation methods [40], where possible. Calculations are performed using Maple.

### III. RESULTS AND DISCUSSION

#### A. Concentric spheres

The behavior of the ELS parameters for a concentric, not fluctuating sphere will be discussed first, as it is the required basis for understanding changes in the structure from this case. The model scattering system is composed of overlapping spheres of different radii, with a core of polystyrene  $n_2 = 1.59$ , surrounded by a mantle simulating a swollen polymer  $n_1 = 1.4$ , layer, placed in an aqueous medium  $n_0 = 1.33$ , with an excitation wavelength of 633 nm. The radius of the core is labeled  $r_c$ , and the thickness of the shell as  $d$ . A minimum of  $\tan \Psi$  occurs at some scattering angle  $\Theta_{\min}$ . This angle is referred to as the Brewster angle [11], with the corresponding value  $(\tan \Psi)_{\min}$ .

Figure 5a shows  $\tan \Psi$  as a function of  $\Theta$  for core-shell particles. Two core sizes are selected, 100 and 120 nm, a size regime where the ELS technique begins to show its sensitivity. The addition of a shell, even one that in this case scatters relatively weakly compared to the core, causes the particle to behave as if it is larger, as expected, seen in

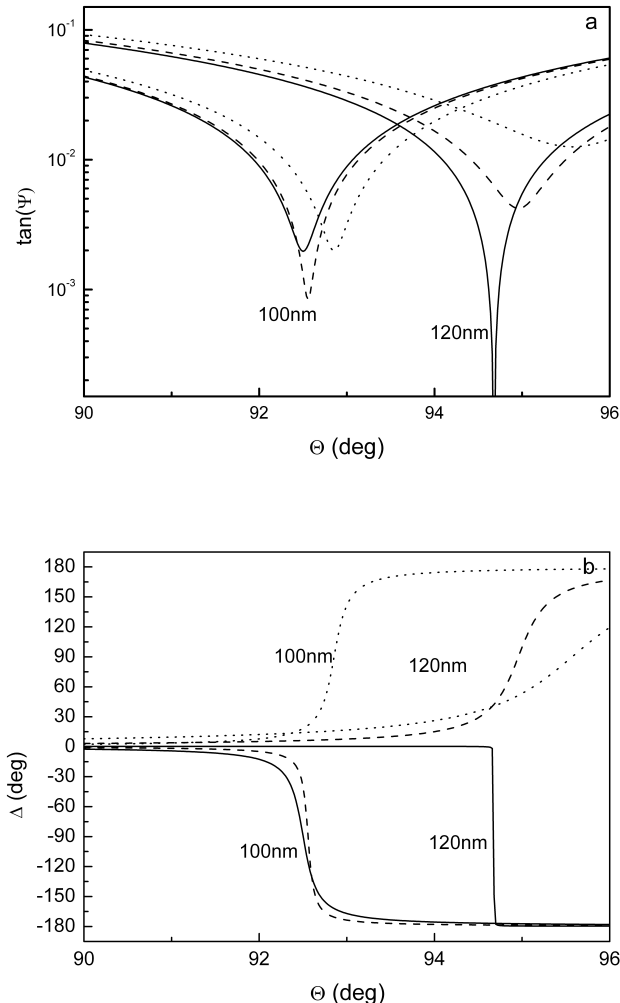


FIG. 5.  $\tan \Psi$  (a) and  $\Delta$  (b) vs. scattering angle  $\Theta$  for concentric spheres of core radius  $r_c = 100$  nm and 120 nm. Shell thicknesses  $d$  of 0 (solid), 20 (dashed), and 40 (dotted) nm.

the shift of  $\Theta_{\min}$ . Considering first the case of a 100nm core, there is a consistent shift of  $\Theta_{\min}$  to higher scattering angles. However, the value of  $(\tan \Psi)_{\min}$  is not so well behaved. For the parameters chosen, there is a decrease in the minimum for the addition of a 20nm shell. Increasing the shell thickness further causes a re-increase in  $(\tan \Psi)_{\min}$ . For the case of the larger core of 120 nm,  $(\tan \Psi)_{\min}$  for the uncoated particle is extremely close to zero, demonstrated by the extremely sharp behavior of  $\tan \Psi$ , while  $\Theta_{\min}$  remains higher than for the 100 nm core.

Figure 5b shows the phase  $\Delta$  as a function of scattering angle for the same sizes and parameters as in Fig. 5a. In general,  $\Delta$  is close to zero degrees for angles below  $\Theta_{\min}$ , and changes sharply through the Brewster angle to approach  $\pm 180^\circ$ . The region of the highest slope in  $\Delta$  corresponds to  $(\tan \Psi)_{\min}$ , and the slope can be correlated to how small  $(\tan \Psi)_{\min}$  is. The inclusion of a shell causes the region with a high slope to shift towards higher scattering angles. The addition of a 20 nm shell to the 100 nm particle, represented by a dashed line, results in a sharper transition, although the transition itself remains at approximately the same angle. This corresponds to a smaller  $(\tan \Psi)_{\min}$  in Fig. 5a. Similarly, for the 120 nm core particle, there is an almost discontinuous change in  $\Delta$ , indicating that  $(\tan \Psi)_{\min}$  is extremely deep in this case. The addition of the coating causes the  $\Delta$  to change more smoothly, as expected for the larger particle.

These effects demonstrate clearly the need for Mie scattering calculations to model ellipsometric light scattering, as changes to the polarization state of the scattered wave are extremely sensitive to small variations of both size and shape. Increasing the core radius from 100 nm to 120 nm causes a significant shift in  $\Theta_{\min}$  to higher scattering angles. An approximate method, such as Rayleigh scattering will capture the existence of a minimum in  $\tan \Psi$  and a sharp

transition of  $\Delta$  at  $90^\circ$ , independent of particle size, an incorrect result for even fairly small particles.

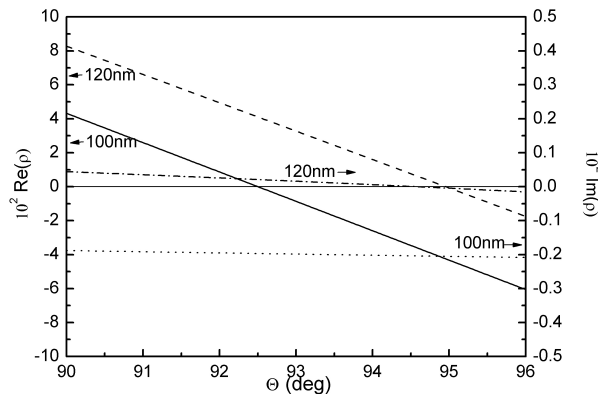


FIG. 6. Real (100 nm, solid and 120 nm, dashed) and imaginary (100 nm, dotted and 120 nm, dot-dash) parts of  $\rho$ . Position of zero is matched on the left and right side vertical axes, and indicated by the horizontal solid line.

Figure 6 shows the real and imaginary parts of  $\rho$  for the uncoated 100 nm and 120 nm spheres, which give insight into the behaviors of  $\tan \Psi$  and  $\Delta$  seen in Fig. 5. As the real part of  $\rho$  passes across zero, the imaginary part remains finite, but very small, causing the phase of the complex ellipsometric ratio to sweep from close to zero degrees to  $\pm 180^\circ$  (see also [15]). The difference in  $\Delta$  is shown between the 100 nm and 120 nm core particles, with the same shell thicknesses. In the case of the 100 nm sphere, the real part of  $\rho$  crosses zero at  $92.5^\circ$  giving  $\Theta_{\min}$ , while  $(\tan \Psi)_{\min}$  has a value corresponding to  $|\text{Im}(\rho)|$  at this point, approximately 0.002. The negative value of  $\text{Im}(\rho)$  gives a negative  $\Delta$  as well.  $\text{Re}(\rho)$  in the case of the 120 nm sphere is similar, while  $\text{Im}(\rho)$  is considerably smaller, and also crosses through zero very close, giving an extremely small value of  $(\tan \Psi)_{\min}$  in this case. For a size where the real and imaginary parts simultaneously cross zero at  $\Theta_{\min}$ ,  $\Delta$  is undefined. The transition of  $\Delta$  from  $0$  to  $\pm 180^\circ$  becomes discontinuous at this point. The occurrence of such a step-like behavior is connected to the switching in the direction of the  $\Theta$  dependent transition parameter variation for the 100 nm core. In Fig. 5b, for example,  $d$  is varied and the  $\Delta$  transition  $0 \rightarrow -180^\circ$  for small  $d$  switches to  $0 \rightarrow +180^\circ$  for larger  $d$ . A step-like behavior of  $\Delta$  is found for a suitable value of  $d$  in between.

While  $\text{Re}(\rho)$  and  $\text{Im}(\rho)$  have a simpler behavior,  $\tan \Psi$  and  $\Delta$  are the parameters measured experimentally, and determine the angular behavior of ELS measurements. The dependence of these parameters on  $r_c$  and  $d$  provides further insight on ELS sensitivity.

To illustrate ELS sensitivity across a wide range of cores sizes, Figs. 7a and 7b show the relationship of  $\Theta_{\min}$  and the corresponding  $(\tan \Psi)_{\min}$  as a function of  $kr_c$ . To compare both different core and shell sizes, the dimensionless ratio of the shell thickness to the core radius is used,  $d/r_c$ . Here,  $\Theta_{\min}$  is obtained using Newton's method. For small values of  $kr_c$ ,  $\Theta_{\min}$  is close to  $90^\circ$  and  $(\tan \Psi)_{\min}$  is small, as expected from a particle that is well approximated by Rayleigh scattering. When  $kr_c$  becomes larger, however, deviations from this approximation are seen. In Fig. 7a, an asymmetric peak occurs, with a continuous rapid change of the position of  $\Theta_{\min}$ . After the main peak,  $\Theta_{\min}$  drops uniformly.

Figure 7b shows the corresponding values of  $(\tan \Psi)_{\min}$ . There is a significant decrease in  $(\tan \Psi)_{\min}$  close to  $kr_c = 1.55$ , while at the same time, the values of  $\Theta_{\min}$  in Fig. 7a change monotonically, explaining the different behavior of the 100 nm and 120 nm core results shown in Fig. 5a. The addition of a shell causes the scattering of the particle to behave as if it were effectively larger than the size of the core indicates. For the 100 nm particle, increasing the shell causes a decrease in  $(\tan \Psi)_{\min}$  at  $kr_c = 1.38$ , while the opposite is seen at  $kr_c = 1.66$ . A extremely deep  $(\tan \Psi)_{\min}$  is also observed at larger core sizes.

Figures 8a and 8b show  $\tan \Psi$  and  $\Delta$  as a function of scattering angle for a particle radius 155.3 nm, corresponding to  $kr_c = 2.05$ . This particular size is selected as it probes the steep slope in Figs. 7a and 7b. For the uncoated particle, the minimum is fairly shallow. For  $d/r_c = 0.1$ , the global minimum has shifted and deepened significantly. Eventually, with increasing shell size, the particle is effectively too large and this minimum disappears again.  $\Delta$ , as seen in Fig. 8b for the same particle size gives further details as to what is occurring. For the uncoated particle,  $\Delta$  crosses through  $90$  degrees as expected at the first minimum, and increases beyond  $180$  degrees, in contrast to what occurs for smaller particles. The reason for this increase is more clear in the larger shell thicknesses, where there is increasingly sharper changes in  $\Delta$ , corresponding to the depth of the minimum.

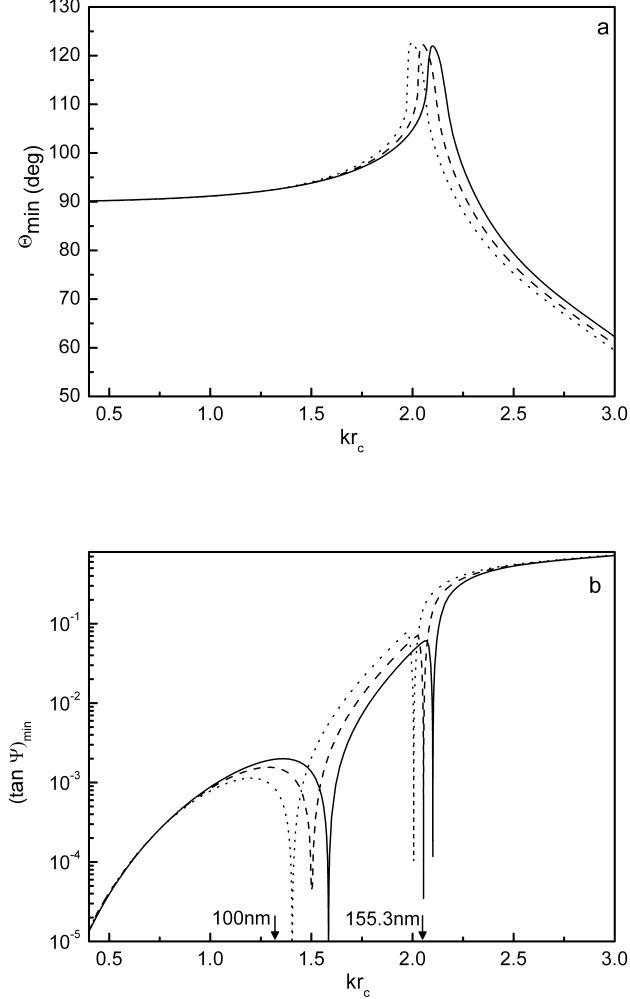


FIG. 7.  $\Theta_{\min}$  (a) and  $(\tan \Psi)_{\min}$  (b) vs.  $kr_c$ , for varying shell sizes. Solid:  $d/r_c = 0$ , dashed:  $d/r_c = 0.1$ , dotted:  $d/r_c = 0.2$ .

Although in Fig. 8b it appears that for large angles, a change in the shell thickness causes  $\Delta$  to go to different angles, these angles differ only by an offset of  $\pm 360^\circ$ .

The origin of these different behaviors can be seen in Fig 9. The polar plot of all five of the different shell thicknesses start in the first quadrant, with a relatively small  $\text{Im}(\rho)$ . For the uncoated particle,  $\text{Re}(\rho)$  goes from positive to negative with a finite and fairly constant  $\text{Im}(\rho)$ . The closest point to the origin reached, in this case where  $\text{Re}(\rho) = 0$ , gives  $\Theta_{\min}$  with corresponding  $(\tan \Psi)_{\min}$ . In the case of  $d/r_c = 0.05$ , however, the curve is a consistent distance from the origin as it passes through the second quadrant, yielding the very broad minimum seen in Fig. 8a for this shell thickness. While  $\text{Re}(\rho)$  crosses zero at similarly for  $d/r_c = 0.1$ , the imaginary part drops off very quickly, such that  $(\tan \Psi)_{\min}$  is very small, and occurs at a different scattering angle from where  $\Delta = 90^\circ$ . With increasing shell thickness, the point where  $\text{Im}(\rho) = 0$  is at increasing values of  $\text{Re}(\rho)$ .

The results for ellipsometric light scattering for concentric spheres gives the required foundation for the discussion of fluctuations. While there is a trend for larger cores to give a Brewster angle at higher scattering angles, the depth of  $(\tan \Psi)_{\min}$ , strongly depends on the actual size and optical properties considered. The overall  $\Theta$  dependence of the experimental parameters  $\tan \Psi$  and  $\Delta$  can be understood through the simpler behavior of  $\text{Re}(\rho)$  and  $\text{Im}(\rho)$ . The location of  $\Theta_{\min}$  corresponds to the transition of  $\text{Re}(\rho)$  through zero, and  $(\tan \Psi)_{\min}$  is equal to  $|\text{Im}(\rho)|$  at this point. The sign of  $\text{Im}(\rho)$  at  $\Theta_{\min}$  is contained in the direction of the  $\Delta$  transition, either  $0^\circ \rightarrow 180^\circ$  for  $\text{Im}(\rho) > 0$ , or  $0^\circ \rightarrow -180^\circ$  for  $\text{Im}(\rho) < 0$ .

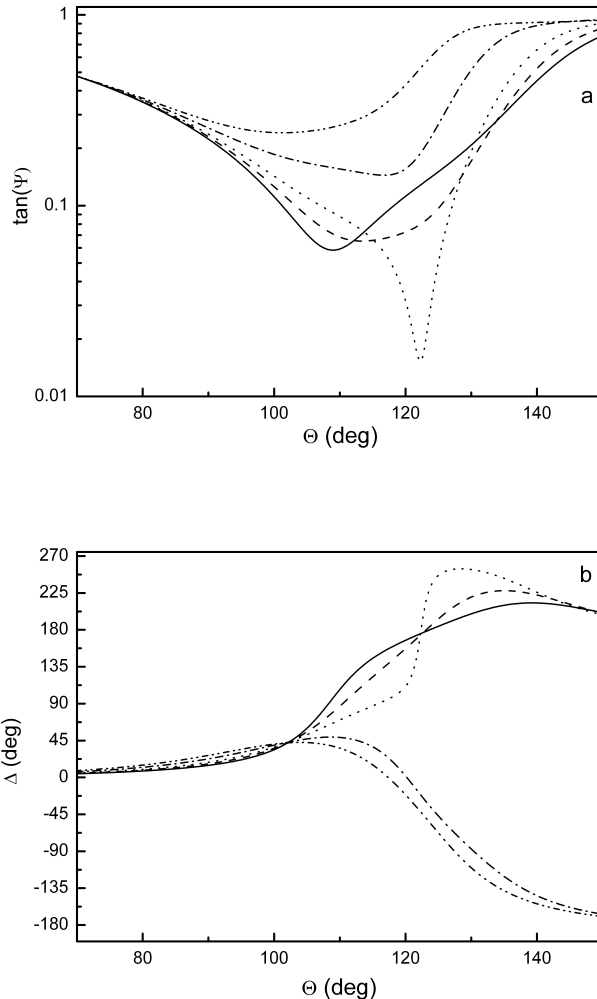


FIG. 8.  $\tan \Psi$  (a) and  $\Delta$  (b) vs. scattering angle for concentric spheres with  $kr_c = 2.05$ .  $d/r_c = 0.0$  (solid),  $d/r_c = 0.05$  (dash),  $d/r_c = 0.1$  (dot),  $d/r_c = 0.2$  (dot-dash),  $d/r_c = 0.3$  (dot-dot-dash)

## B. Concentric Fluctuations

Concentric fluctuations are considered to be those where the softer shell of a core-shell particle changes in size symmetrically, so that derivatives with respect to the shell thickness  $d$  can be taken. The index of refraction is varied as described in equations (8) and (10). The contrast term used in the calculations is  $n_1 - n_0 = 0.07$ .

The derivatives of  $\tan \Psi$  and  $\Delta$  for 100 and 120nm cores are shown in Figs. 10a and 10b respectively, for two different relative shell thicknesses. For the case of the 100 nm particles, the derivatives of  $\tan \Psi$  are fairly constant over the scattering angle except for a transition from a negative to a positive derivative near  $(\tan \Psi)_{\min}$ . The magnitude of the derivative is almost identical between the two shell sizes, due to a balance between the increase in size and the decrease in contrast, although there is a difference in slope. The particles with a slightly larger core have a similar trend in  $(\tan \Psi)'$  in that the derivative crosses zero in the region of the minimum in  $\tan \Psi$ . The variation of  $(\tan \Psi)'$  is also sharper in the case of shell of  $d/r_c = 0.1$ , corresponding to the deeper  $(\tan \Psi)_{\min}$ . These derivatives can be thought of as moving  $\Theta_{\min}$  to smaller scattering angles in both cases.

The derivatives of  $\Delta$  in Fig. 10b show a peak close to the Brewster angle, indicating that the sharp variation of  $\Delta$  with respect to scattering angle at this point is highly sensitive to small changes in structure. Away from the Brewster angle, however, the derivatives are relatively small. For the 100 nm core, the magnitude of  $\Delta'$  is considerably higher for the larger shell, and the negative sign indicates that for an increasing shell thickness, the minimum in  $\tan \Psi$  is

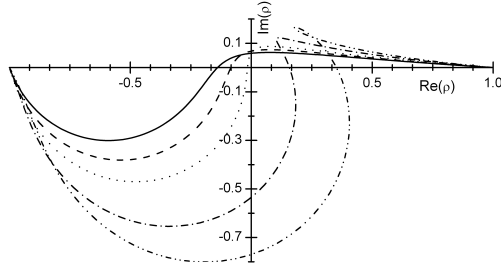


FIG. 9. Polar plot of  $\text{Im}(\rho)$  vs.  $\text{Re}(\rho)$  for concentric spheres  $kr_c = 2.05$ .  $d/r_c = 0.0$  (solid),  $d/r_c = 0.05$  (dash),  $d/r_c = 0.1$  (dot),  $d/r_c = 0.2$  (dot-dash),  $d/r_c = 0.3$  (dot-dot-dash), over scattering angles from  $0^\circ$  to  $180^\circ$

smaller, correlating to a sharper shift in  $\Delta$  through the Brewster angle. The opposite is true in the case of the 120 nm core, where  $\Delta$  is a smoother function of scattering angle, causing a decrease in  $\Delta$  for a larger shell. The opposite direction between the 100nm and 120nm core cases are caused by the difference in phase direction, as seen in 5b.

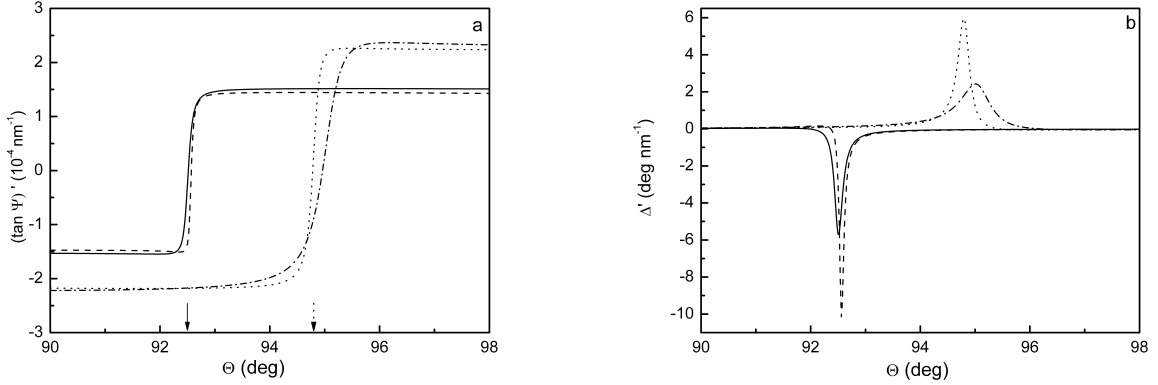


FIG. 10.  $\frac{d(\tan \Psi)}{dd}$  (a) and  $\frac{d(\Delta)}{dd}$  (b) vs. scattering angle for a particle of 100 nm core with a shell of thickness  $d/r_c = 0.1$  (solid),  $d/r_c = 0.2$  (dashed), and 120 nm core with a shell of  $d/r_c = 0.1$  (dotted),  $d/r_c = 0.2$  (dot-dash). Solid and dotted arrows represent  $\Theta_{\min}$  for 100 nm and 120 nm spheres with shell thickness  $d/r_c = 0.1$ , respectively.

Derivatives of  $\tan \Psi$  and  $\Delta$  for larger cores of 155.3 nm, corresponding to  $kr_c = 2.05$  are shown in Figs. 11a and 11b respectively, for parameters matching those shown in Figs. 8a and 8b. The derivatives of the ellipsometric variables are more complex than those of the smaller particles. For the  $d/r_c = 0.1$  shell, which had very small  $(\tan \Psi)_{\min}$ , the derivative is positive in the vicinity of  $(\tan \Psi)_{\min}$ . The negative derivative in the case of  $d/r_c = 0.2$  shows that the scattering is moving towards smaller values of  $(\tan \Psi)_{\min}$  for increasing shell size. The derivative of  $\Delta$  shows more clearly that  $\Theta_{\min}$  moves to lower scattering angles. The strong negative and positive peaks in the case of  $d/r_c = 0.1$  compared to  $d/r_c = 0.2$  show that the slope of  $\Delta$  is steeper for the thinner shell, and that there exists high sensitivity to changes in structure.

For the detection of fluctuations in an experiment, the results of this section show that the relative contrast is largest close to  $\Theta_{\min}$ . For smaller particles, there is a strong peak in the derivative for  $\Delta$ , the scattering angle and magnitude of which can be tuned through adjustment of core radius or the wavelength of incident radiation. Larger particles show a smaller peak in  $\Delta'$ , but much larger values of  $(\tan \Psi)'$ .

### C. Nonconcentric Fluctuations

The variation of  $\tan(\Psi)$  as a function of scattering angle for nonconcentric spheres is shown in Fig. 12 for a displacement of 5 nm along the three cardinal axes. In general, when the displacement is in the scattering plane, in either the  $z$  (along the incident beam) or  $x$  (perpendicular to the incident beam), the effect is similar, in that there is an increase in  $\tan(\Psi)$ , the characteristics of which is discussed below. In the case of displacement perpendicular to

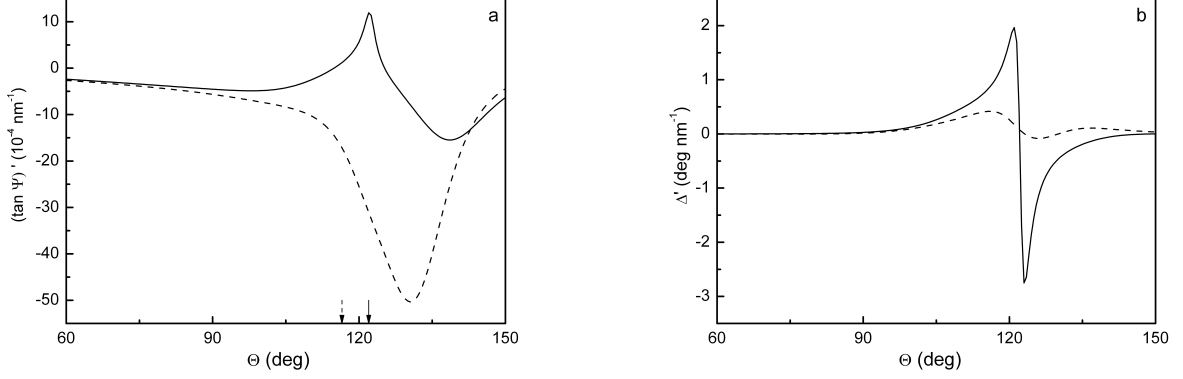


FIG. 11.  $\frac{d(\tan \Psi)}{r_c}$  (a) and  $\frac{d(\Delta)}{r_c}$  (b) vs. scattering angle for particles with a core of  $x=2.05$ , with shell of thickness  $d/r_c = 0.1$  (solid),  $d/r_c = 0.2$  (dashed). Solid and dashed arrows represent  $\Theta_{\min}$  for shell thickness  $d/r_c = 0.1$  and  $d/r_c = 0.1$ , respectively.

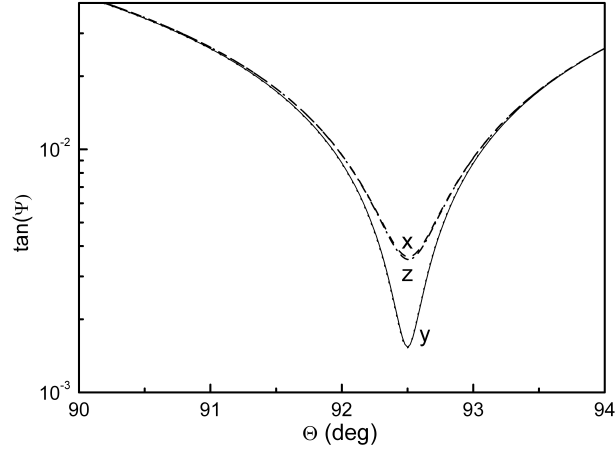


FIG. 12.  $\tan \Psi$  vs. scattering angle for spheres of core radius 100 nm, shell of thickness 10 nm, for concentric spheres (solid) and for shifts of 5nm along the  $x$  (dashed),  $y$  (dotted), and  $z$  (dot-dash). The incident beam is directed along the  $z$  axis and the scattering plane is defined as the  $xz$  plane. The results for the concentric and a shift in the  $y$  direction cases cannot be clearly distinguished on this scale.

the scattering plane ( $y$  direction), the effects at  $\Theta_{\min}$  are tiny. There is a shift of the minimum in  $\tan(\Psi)$  to slightly higher scattering angles, and as well, a deepening of the minimum.

The derivative of  $\tan(\Psi)$  as a function of  $h$ , the separation between centers, is shown in Fig. 13a. As illustrated here, the behaviour of  $\tan(\Psi)$  for displacements in the scattering plane ( $x$  and  $z$  directions) is extremely similar, with a peak derivative at a scattering angle slightly higher than  $(\tan \Psi)_{\min}$  in the concentric case. The behaviors of the derivative in  $x$  and  $z$  can be understood to arise from the breaking of the scattering symmetry that occurs in concentric particle.

For the  $y$  direction, the situation is quite different. The value of  $\tan(\Psi)$  changes asymmetrically as a function of scattering angle, decreasing for angles lower than the minimum in  $\tan(\Psi)$  and increasing for higher angles, causing the net shift to higher scattering angles as seen in Fig. 12. It is interesting to note that this function crosses zero close to  $(\tan \Psi)_{\min}$ , similar to the results for symmetric fluctuations (see Fig. 10). Here, the geometry of the compound particle, as seen by light polarized in the horizontal direction, does not deviate much for small shifts. So therefore, at the minimum in  $\tan(\Psi)$ , where the Jones matrix element for the horizontal case  $S_2$  is at a minimum, the changes brought about in  $S_1$  due to the shift have little effect. Comparing this behavior to the results for concentric fluctuations, the derivative in the  $y$  direction can be understood to be a shrinking of the thickness of the shell as observed by the light.

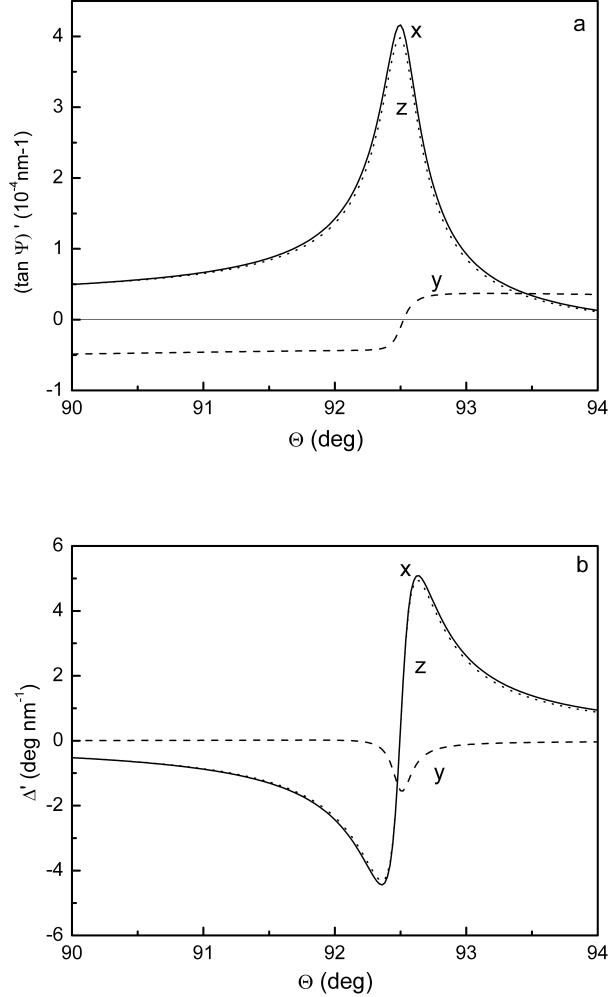


FIG. 13.  $\frac{d(\tan \Psi)}{dh}$  (a) and  $\frac{d\Delta}{dh}$  (b) vs. scattering angle for spheres of core radius 100 nm, shell of thickness 10 nm, for shifts along the 3 cardinal axes. The incident beam is directed along the z axis.

This effect causes a different trend as well as a smaller derivative than those observed for in-plane noncentricity, as well as a behavior similar to that of a shell decreasing in thickness. This behavior implies that that observation of noncentricity in the  $y$  direction requires measurement at scattering angles away from  $(\tan \Psi)_{\min}$ .

The derivatives of  $\Delta$  follow a similar pattern, as seen in Fig. 13b. The in plane cases show  $\Delta$  changing according to a function which is reminiscent of the curves obtained from derivatives of a negative peak, with an increasing negative slope followed by increase, and a crossing through zero, which occurs at the Brewster angle.

The derivatives of  $\tan(\Psi)$  and  $\Delta$  as a function of scattering angle for larger particles are shown in Figs. 14a and 14b respectively. The same core size as the results in Figs. 8a and 8b is used, and the shell thickness is  $d/r_c = 0.1$ . In contrast to the results for 100 nm particles, the derivatives are no longer simple, but show large scale variations over the entire scattering range. As for smaller particles, the derivative for in-plane noncentricity show a similar behavior in both directions. The derivatives of  $\tan(\Psi)$ , in a behavior opposite to that seen in the smaller particles, are small close to this point, but are significant at both, larger and smaller scattering angles from the minimum.

The derivative of  $\Delta$ , on the other hand, shows a strong peak at  $(\tan \Psi)_{\min}$ , reflecting that as this region has fairly large change in  $\Delta$  as a function of scattering angle, a slight movement away from concentricity causes a significant change in  $\Delta$ . The magnitude of the derivatives, however, especially for a nonconcentric shift in the  $y$  direction, are dependent on the specific size. In this specific instance, there is a strong resonance, and larger derivatives in  $\tan(\Psi)$  are observed slightly away from the minimum in  $\tan(\Psi)$  as the resonance shifts to lower scattering angles in the in plane case and the higher scattering angles in the out of plane case. In both of these possibilities, the derivative

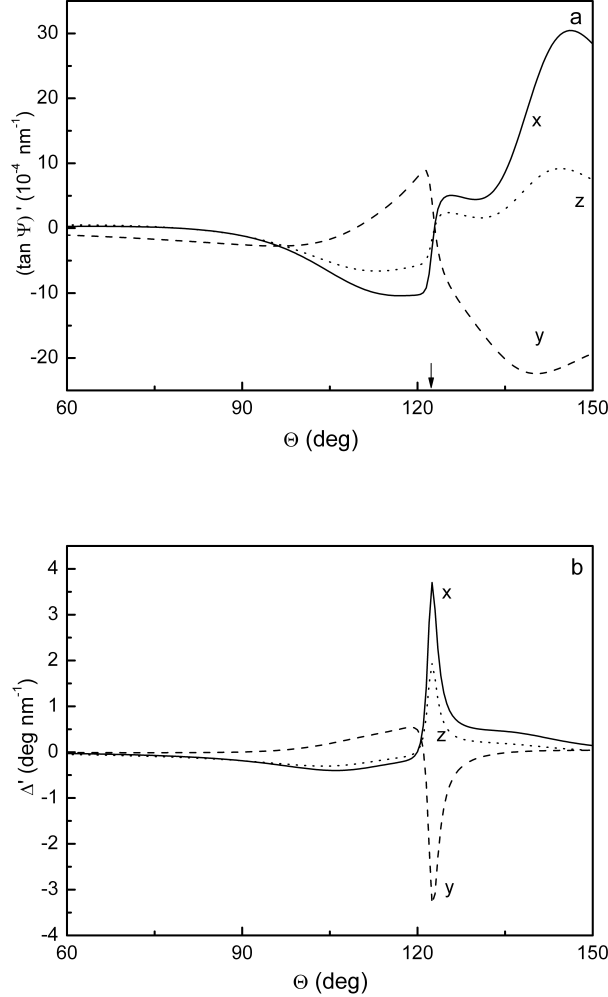


FIG. 14.  $\frac{d(\tan(\Psi))}{dh}$  (a) and  $\frac{d\Delta}{dh}$  (b) vs. scattering angle for spheres of core of  $kr_c=2.05$ , shell thickness of  $d/r_c = 0.1$ , for shifts along the 3 cardinal axes. The arrow in (a) marks the position of  $\Theta_{\min}$ .

of  $\Delta$  is peaked at the minimum as the change in phase varies quickly as the resonance is probed. The results for both smaller and larger particles show a wide variety in the character and magnitude of scattering derivatives for the different directions, showing a need for detailed calculations for concentric and nonconcentric scattering systems.

The derivatives at  $\Theta_{\min}$  as functions of the  $kr_c$  for both concentric and nonconcentric fluctuations are seen in Fig. 15. For extremely small particles, the rate of change in  $\tan \Psi$  for NCFs is considerably greater than for CFs. The behavior for the nonconcentric cases are similar, for larger cores,  $(\tan \Psi)'_{\min}$  in the x direction is slightly larger than in the z.

The direction of the derivatives change in the region of  $kr_c = 1.4$ , due to the deep  $(\tan \Psi)_{\min}$  occurring as seen in Fig. 7b. The small negative values of  $(\tan \Psi)'_{\min}$  for  $kr_c < 1.4$  can then be interpreted as moving toward the infinitely small  $(\tan \Psi)_{\min}$  seen in the Rayleigh regime, and the NCFs tend to move the scattering away from this ideal case.

In the region near  $kr_c = 2.0$ , there are extremely rapid changes in the derivative in all cases. This behavior is due to the sudden decrease in  $\tan \Psi$  at the same region Fig. 7b. In this highly sensitive region, small changes in structure cause large derivatives.

The derivatives of ellipsometric variables for nonconcentric shifts show different behavior for nonconcentricity in the plane and out of the plane. In particular, the out of plane results are similar to those seen for concentric fluctuations (see Figs. 13 and 10). The derivatives of  $\Delta$  show distinct peaks for the sizes considered here, and may be a more useful parameter for initial detection of such shifts, as these peaks appear consistently regardless of size or direction of nonconcentricity. For small cores, the concentric fluctuations and nonconcentric fluctuations out of plane are

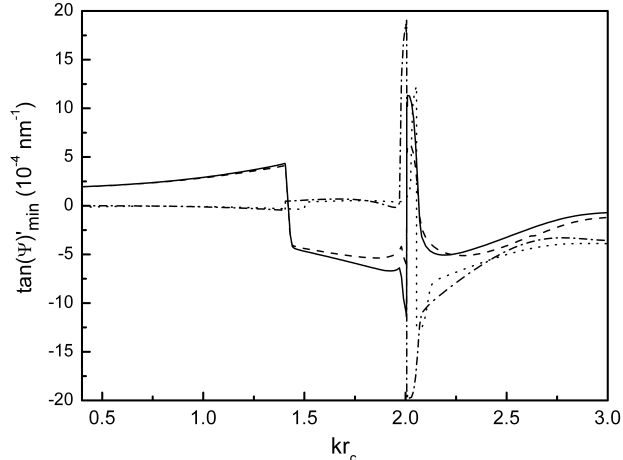


FIG. 15.  $((\tan \Psi)_{\min})'$  as a function of  $kr_c$  at  $\Theta_{\min}$ , for nonconcentric fluctuations of in the x (solid) and z (dashed) directions, for a shell thickness  $d/r_c = 0.2$ , and concentric fluctuations of shell thickness  $d/r_c = 0.1$  (dotted) and  $d/r_c = 0.2$  (dot-dash).

considerably smaller than the nonconcentric shifts in plane, although they approach similar magnitudes for larger particles. At values of  $kr_c$  where  $(\tan \Psi)_{\min}$  is extremely small, the highest derivatives of  $\tan \Psi$  appear, suggesting that for a specific size, the choice of wavelength of incident light can be critical to achieve higher observable contrast for fluctuations in an experiment.

#### IV. CONCLUSIONS

Fluctuations in size and shape is an integral part of the physics of soft particles. The ability to characterize changes during such fluctuations gives information beyond that of observation of equilibrium or average structures. To this end, a method to find the derivatives of the Jones matrix elements is described, allowing for the computation of analytical derivatives for scattering observables to arbitrary accuracy and high order derivatives. Through formal differentiation of the order of scattering method, derivatives can be taken without the need for matrix inversion at any step, simplifying both the computation and interpretation of results. The derivatives are related to the contrast, the change in scattering observables as a function of structure.

Ellipsometric light scattering shows a sensitivity to changes across a range of particle sizes, and, by extension, contrast. In a measurement close to the Brewster angle, small changes in size or contrast can cause very large derivatives in the ELS parameters, leading further to large derivatives in  $\Delta$ . Mie scattering calculations are required to treat the equilibrium case to provide a useful comparison to realistic particles. In order to capture changes in structure away from the equilibrium with reliability, exact treatment is again the required tool. Modeled ellipsometric light scattering for concentric particles is performed to obtain a base understanding of the behavior of small and large colloidal scatters. The derivatives of ellipsometric light scattering parameters are calculated for concentric and nonconcentric fluctuations in a frame fixed to that of the laboratory, allowing further breaks in symmetry without significantly extra computation effort.

The changes in the ellipsometric light scattering results for both concentric and nonconcentric fluctuations have a rich and varied profile, strongly dependent on size and optical properties, as well as fluctuation mode and direction. Depending on the size and optical properties of the system, derivatives of ELS parameters can be found that might be large enough for experimental detection of fluctuations.

The computed results for both the ellipsometric light scattering as well as the derivatives is currently being used to guide novel experiments to measure the fluctuations of core-shell particle suspension.

## ACKNOWLEDGMENTS

Financial support of the Swiss National Science Foundation, NSF Project number 200021\_126849/1 is gratefully acknowledged. The support of the Adolphe Merkle Institute is also acknowledged.

### Appendix

The vector spherical harmonics at some positions  $\mathbf{R}$  are [38]

$$\mathbf{N}_{mn1}(\mathbf{R}) = e^{im\phi} \begin{pmatrix} \frac{z_n(kR)}{kR} n(n+1) P_n^m(\cos\theta) \hat{r} \\ \frac{1}{kR} \frac{\partial [R z_n(kR)]}{\partial R} \tau_{mn}(\cos\theta) \hat{\theta} \\ i \frac{1}{kR} \frac{\partial [R z_n(kR)]}{\partial R} \pi_{mn}(\cos\theta) \hat{\phi} \end{pmatrix} \quad (\text{A.1})$$

$$\mathbf{N}_{mn2}(\mathbf{R}) = e^{im\phi} \begin{pmatrix} 0 \\ z_n(kR) \pi_{mn}(\cos\theta) \hat{\theta} \\ -z_n(kR) \tau_{mn}(\cos\theta) \hat{\phi} \end{pmatrix}, \quad (\text{A.2})$$

where  $\hat{r}, \hat{\theta}, \hat{\phi}$  are the unit vectors in spherical coordinates in the frame of the incident light,  $z_n(kR)$  are the spherical Bessel functions, with  $R = |\mathbf{R}|$ . The  $P_n^m(\cos\theta)$  are the associated Legendre polynomials of the first kind [39], defined by

$$P_n^m(x) = (-1)^m (1-x^2)^{m/2} \frac{d^m P_n(x)}{dx^m} \quad (\text{A.3})$$

where  $P_n(x)$  are the Legendre Pynomials. The angular functions are given by:

$$\tau_{mn}(\cos\theta) = \frac{d}{d\theta} P_n^m(\cos\theta) \quad (\text{A.4})$$

$$\pi_{mn}(\cos\theta) = \frac{m}{\sin\theta} P_n^m(\cos\theta). \quad (\text{A.5})$$

The kind of spherical Bessel function depends on the specific usage. The spherical Bessel function of the third kind  $h_1(kR)$  is used to find the Jones matrix elements. Their use in the derivation of the translation coefficients is discussed in excellent detail elsewhere [24, 26, 36, 38].

Although it is often convenient to define the reference frame of the system to take advantage of the symmetry of the scattering system, the formalism here defines the reference frame from the incident and scattered light [38, 41]. While this choice requires all possible angular momenta to be considered, there are two major benefits. The first is that a simpler correlation with experiments is allowed, as the scattering angle is directly correlated to the azimuthal angle in spherical coordinates. The second is that further breaks in the symmetry do not cause extra complication aside from the need to consider more interactions. For example, multiple inclusions surrounded by a single shell would not require significant change to the equations.

The expansion coefficients of the plane wave are given in general by [38]

$$p_{mnp}(\theta, \phi, \gamma) = -(-1)^m i^{n+1} \frac{2n+1}{2} e^{-im\phi} \\ \times \left( \frac{1}{n(n+1)} D_{mn}^1(\theta) e^{-i\gamma} + (-1)^p D_{mn}^{-1}(\theta) e^{i\gamma} \right), \quad (\text{A.6})$$

where the  $D_{mn}^k$  functions are related to the generalized spherical functions [38, 42]. They can be calculated through

$$D_{mn}^0(\theta) = (-1)^m P_n^{-m}(\cos\theta) \quad (\text{A.7})$$

and then using recursion through

$$D_{mn}^{k+1}(\theta) = \cos^2\left(\frac{\theta}{2}\right) D_{m-1n}^k - (n-m)(n+m+1) \\ \times \sin^2\left(\frac{\theta}{2}\right) D_{m+1n}^k - k \sin(\theta) D_{mn}^k(\theta) \quad (\text{A.8})$$

and

$$D_{mn}^{-k}(\theta) = (-1)^{k+m} \frac{(n-m)!(n-k)!}{(n+m)!(n+k)!} D_{-mn}^k(\theta) \quad (\text{A.9})$$

For the case where the incident angle  $\theta$  is constrained to lie along the z-axis, the  $D_{mn}^k$  simplify to:

$$D_{m,n}^{(k)}(0) = \delta_{k,m} \quad (\text{A.10})$$

and the expansion coefficients to:

$$p_{1np}(0, 0, \gamma) = i^{n+1} \frac{2n+1}{2n(n+1)} e^{-i\gamma}, \quad (\text{A.11})$$

$$p_{-1np}(0, 0, \gamma) = i^{n+1} \frac{2n+1}{2} (-1)^p e^{i\gamma} \quad (\text{A.12})$$

The angle  $\gamma$  is the polarization angle of the incident electric field, relative to the scattering ( $xz$ ) plane.

The relation between the two different centers are given by the interaction coefficients  $A_{mnp\mu\nu q}^{\ell\ell'}$ , which represent the change of basis of the vector spherical harmonics from origin  $\ell$  to origin  $\ell'$ . In the laboratory frame of reference,  $R_{\ell\ell'}$ ,  $\Theta_{\ell\ell'}$ ,  $\Phi_{\ell\ell'}$  represent the position of the center of sphere  $\ell$  relative to sphere  $\ell'$ . The interaction coefficients are given by

$$A_{mnp\mu\nu q}^{\ell\ell'} = -i^{n-\nu} (-1)^m (2n+1) \sum_w i^w C_{-mn\mu\nu}^w C_{-1n1\nu}^w j_w(kR_{\ell\ell'}) P_w^{\mu-m}(\cos \Theta_{\ell\ell'}) \exp[i(\mu-m)\Phi_{\ell\ell'}], \quad (\text{A.13})$$

where  $j_w$  are the spherical Bessel functions of the first kind, and the  $C_{-mn\mu\nu}^w$  are coupling coefficients related to the momentum coupling [38]. The summation over  $w$  is taken from  $|\mu-m|$  or  $|\nu-n|$ , whichever is lower, to  $n+\nu$ , and includes even  $n+\nu+w$  when  $p=q$ , and odd  $n+\nu+w$  otherwise. A useful symmetry relation is:

$$A_{mnp\mu\nu q}^{\ell'\ell} = (-1)^{n+\nu+q+p} A_{mnp\mu\nu q}^{\ell\ell'} \quad (\text{A.14})$$

The  $C_{mn\mu\nu}^w$  terms are related to the Wigner 3j coefficients by:

$$C_{mn\mu\nu}^w = \left( \frac{(n+m)!(\nu+\mu)!(w-m-\mu)!}{(n-m)!(\nu-\mu)!(w+m+\mu)!} \right)^{1/2} \\ \times \frac{(-1)^{n+\nu-m-\mu}}{\sqrt{2w+1}} \begin{pmatrix} n & \nu & w \\ m & \mu & -m-\mu \end{pmatrix} \quad (\text{A.15})$$

where the Wigner 3j symbol is calculated through recursion [43].

As the only term dependent on the distance between the spherical centers,  $h$ , is the spherical Bessel function  $j_w(h)$ , the derivatives of the interaction coefficients are not much more complicated.

The Mie coefficients are reproduced here for completeness.  $\bar{a}_{np}^{\ell}$  and  $\bar{c}_{np}^{\ell}$  represent the external and internal scattering coefficients, respectively, for a field impinging externally, or on a convex surface.  $\hat{a}_{np}^{\ell}$  and  $\hat{c}_{np}^{\ell}$  are used for the case of a convex surface, or in this case, light scattered from the core illuminating the internal surface of the shell. The relative index of refraction used,  $m_{\ell}$ , is the index of refraction of the scatterer in question,  $n_{\ell}$ , relative to the medium immediately surrounding it,  $n_{\ell-1}$ . For instance, for the core shell system depicted in Fig. 1,  $m_2 = n_2/n_1$ , and  $m_1 = n_1/n_0$ . The amplitude of the wavevector is defined as  $k = n_0 k_0$ ,  $k_0 = 2\pi/\lambda$  is the wavenumber in vacuum, and  $n_0$  is the index of refraction the medium surrounding the particle under consideration. The prime notation indicates differentiation with respect to the argument of the function.  $\psi_n(kr)$  and  $\xi_n(kr)$  are the Ricatti-Bessel functions of the first and third kind, respectively.

$$\bar{a}_{n1}^\ell = -\frac{m_\ell \psi_n'(kr) \psi_n(m_\ell kr) - \psi_n(kr) \psi_n'(m_\ell kr)}{m_\ell \xi_n'(kr) \psi_n(m_\ell kr) - \xi_n(kr) \psi_n'(m_\ell kr)}, \quad (\text{A.16})$$

$$\bar{a}_{n2}^\ell = -\frac{m_\ell \psi_n(kr) \psi_n'(m_\ell kr) - \psi_n'(kr) \psi_n(m_\ell kr)}{m_\ell \xi_n(kr) \psi_n'(m_\ell kr) - \xi_n'(kr) \psi_n(m_\ell kr)}, \quad (\text{A.17})$$

$$\bar{c}_{n1}^\ell = -\frac{im_\ell \bar{a}_{n1}}{m_\ell \psi_n'(kr) \psi_n(m_\ell kr) - \psi_n(kr) \psi_n'(m_\ell kr)}, \quad (\text{A.18})$$

$$\bar{c}_{n2}^\ell = \frac{im_\ell \bar{a}_{n2}}{m_\ell \psi_n(kr) \psi_n'(m_\ell kr) - \psi_n'(kr) \psi_n(m_\ell kr)}, \quad (\text{A.19})$$

$$\hat{a}_{n1}^\ell = -\frac{m_\ell \xi_n'(kr) \xi_n(m_\ell kr) - \xi_n(kr) \xi_n'(m_\ell kr)}{m_\ell \xi_n'(kr) \psi_n(m_\ell kr) - \xi_n(kr) \psi_n'(m_\ell kr)}, \quad (\text{A.20})$$

$$\hat{a}_{n2}^\ell = -\frac{m_\ell \xi_n(kr) \xi_n'(m_\ell kr) - \xi_n'(kr) \xi_n(m_\ell kr)}{m_\ell \xi_n(kr) \psi_n'(m_\ell kr) - \xi_n'(kr) \psi_n(m_\ell kr)}, \quad (\text{A.21})$$

$$\hat{c}_{n1}^\ell = \frac{i}{m_\ell \xi_n'(kr) \psi_n(m_\ell kr) - \xi_n(kr) \psi_n'(m_\ell kr)}, \quad (\text{A.22})$$

$$\hat{c}_{n2}^\ell = -\frac{\xi_n'(m_\ell kr) \psi_n(m_\ell kr) - \xi_n(m_\ell kr) \psi_n'(m_\ell kr)}{m_\ell \xi_n(kr) \psi_n'(m_\ell kr) - \xi_n'(kr) \psi_n(m_\ell kr)}. \quad (\text{A.23})$$

- 
- [1] D. F. Evans and H. Wennerström, *The Colloidal Domain: Where Physics, Chemistry, Biology, and Technology Meet*, 2nd ed.
  - [2] I. K. Voets, A. de Keizer, P. M. Frederik, R. Jellema, and M. A. C. Stuart, *J. Colloid Interf. Sci.* **339**, 317 (2009).
  - [3] D. Vlassopoulos and G. Fytas, *Adv. Polym. Sci.* **236**, 1 (2010).
  - [4] J. Oberdisse, P. Hine, and W. Pyckhout-Hintzen, *Soft Matter* **3**, 476 (2007).
  - [5] M. Guo and H. M. Wyss, *Macromol. Mater. Eng.* **296**, 223 (2011).
  - [6] R. Bubeck, P. Leiderer, and C. Bechinger, *Europhys. Lett.* **60**, 474 (2002).
  - [7] M. Kong, B. Partoens, A. Matulis, and F. M. Peeters, *Phys. Rev. E* **69**, 036412 (2004).
  - [8] S. Bolisetty, M. Hoffmann, S. Lekkala, T. Hellweg, M. Ballauff, and L. Harnau, *Macromolecules* **242**, 1264 (2009).
  - [9] K.-K. Liu, *J. Phys. D* **39**, R189 (2006).
  - [10] A. A. Riziq, M. Trainic, C. Erlick, E. Segre, and Y. Rudichl, *Atmos. Chem. Phys.* **8**, 1823 (2008).
  - [11] A. Erbe, K. Tauer, and R. Sigel, *Phys. Rev. E* **73**, 031406 (2006).
  - [12] A. Erbe, K. Tauer, and R. Sigel, *Langmuir* **23**, 452 (2007).
  - [13] A. Erbe and R. Sigel, *Eur. Phys. J. E* **22**, 303 (2007).
  - [14] A. Erbe and R. Sigel, *Appl. Opt.* **47**, 2161 (2008).
  - [15] A. Erbe, K. Tauer, and R. Sigel, *Langmuir* **25**, 2703 (2009).
  - [16] A. Erbe and R. Sigel, in *EPJ Web of Conferences, V. 5*, edited by E. Garcia-Caurel and A. de Martino (2010).
  - [17] R. Sigel, *Curr. Opin. Colloid Interface Sci.* **14**, 426 (2009).
  - [18] C. Wu, S. Zhou, S. C. F. Au-yeung, and S. Jiang, *Angew. Makromol. Chem.* **240**, 123 (1996).
  - [19] C. F. Bohren and D. R. Huffman, *Absorption and Scattering of Light by Small Particles* (Wiley, 1983).
  - [20] M. Kerker, *The Scattering of Light* (Academic, 1969).
  - [21] G. Mie, *Ann. Phys.* **25**, 377 (1908).
  - [22] J. G. Fikioris and N. K. Uzunoglu, *J. Opt. Soc. Am.* **69**, 1359 (1979).
  - [23] D. Ngo, G. Videen, and P. Chylek, *Comput. Phys. Commun.* **1077**, 94 (1996).
  - [24] K. A. Fuller, *J. Opt. Soc. Am. A* **12**, 893 (1995).
  - [25] F. Borghese, P. Denti, R. Saija, and O. I. Sindoni, *J. Opt. Soc. Am. A* **9**, 1327 (1993).
  - [26] G. Gouesbet, *J. Quant. Spectrosc. Radiat. Transfer* **110**, 1223 (2009).
  - [27] F. Xu and A. B. Davis, *Opt. Lett.* **36**, 4464 (2011).
  - [28] R. Spurr, J. Wang, J. Zeng, and M. Mishchenko, *Journal of Quantitative Spectroscopy and Radiative Transfer* **113**, 425 (2012).
  - [29] J. J. Wang, G. Gouesbet, Y. P. Han, and G. Gréhan, *J. Opt. Soc. Am. A* **28**, 24 (2011).
  - [30] J. J. Wang, G. Gouesbet, G. Gréhan, Y. P. Han, and S. Saengkaew, *J. Opt. Soc. Am. A* **28**, 1849 (2011).
  - [31] B. Friedman and J. Russek, *Q. Appl. Math.* **12**, 13 (1954).
  - [32] S. Stein, *Q. Appl. Math.* **19**, 15 (1961).
  - [33] O. R. Cruzan, *Q. Appl. Math.* **20**, 33 (1962).
  - [34] M. C. Chen, S. D. Tsai, M. R. Chen, S. Y. Ou, W.-H. Li, and K. C. Lee, *Phys. Rev. B* **51**, 4507 (1995).
  - [35] J. H. Bruning and Y. Lo, *IEEE Trans. Antennas Propag.* **19**, 378 (1971).
  - [36] L. Boyde, K. J. Chalut, and J. Guck, *Phys. Rev. E* **83**, 026701 (2011).
  - [37] D. W. Mackowski and M. I. Mishchenko, *Phys. Rev. A* **83**, 013804 (2011).
  - [38] M. I. Mishchenko, J. W. Hovenier, and L. D. Travis, *Light Scattering by Nonspherical Particles: Theory, Measurements, and Applications* (Academic, 2000).
  - [39] M. Abramowitz and I. A. Stegun, *Handbook of Mathematical Functions with Formulas, Graphs, and Mathematical Tables* (Dover Publications, New York, 1964).
  - [40] B. Draine and P. Flatau, *J. Opt. Soc. Am. A* **11**, 1491 (1994).
  - [41] M. I. Mishchenko, L. D. Travis, and A. A. Lacis, *Scattering, Absorption, and Emission of Light by Small Particles* (Cambridge University Press, 2002).
  - [42] M. I. Mishchenko, L. D. Travis, and D. W. Mackowski, *J. Quant. Spectrosc. Radiat. Transfer* **55**, 535 (1996).
  - [43] J. H. Luscombe and M. Luban, *Phys. Rev. E* **57**, 7274 (1998).